Pergamon

0301-9322(95)00035-6

Int. J. Multiphase Flow Vol. 21, No. 6, pp. 1123–1140, 1995

0301-9322/95 $9.50 + 0.00

FORMATION OF WAVES ON A HORIZONTAL ERODIBLE BED OF PARTICLES

W. C. KURU, D. T. LEIGHTON and M. J. McCREADY
Department of Chemical Engineering, University of Notre Dame, Notre Dame, IN 46556, U.S.A.

(Received 5 August 1994; in revised form 26 April 1995)

Abstract—The mechanisms responsible for the initial growth of sand waves on the surface of a settled layer of particles are studied experimentally and theoretically. Experiments employ water–glycerin solutions of 1–14 cP and glass spheres ($\rho_s = 2.4\ g/cm^3$) that are either 100 or 300 μm in diameter. The particle Reynolds number and Shields parameter are of order one and the flow Reynolds number is of order 1000 to 10,000. Experimentally obtained regime maps of sand wave behavior and data on the wavelengths of the sand waves that first appear on the surface of the settled bed are presented. Turbulence in the clear liquid is not necessary for formation of waves and there is no dramatic change in behavior as the flowrate is increased across the turbulent transition. The initial wavelength varies as the Froude number to the first power. Because a flowing suspension phase is observed before waves form, linear stability analysis of the clear-layer–suspension-layer cocurrent two-phase flow is presented. The suspension phase is modeled as a continuum that has an either constant or exponentially increasing viscosity. Neither of the models correctly predicts the wavelength for the first observed waves, their growth rate or their speed. However, the initial wavelength is found to agree well with the trajectory length for a saltating particle obtained from a model for forces on individual particles.

Key Words: particle transport, dune formation, particle resuspension, saltation

1. INTRODUCTION

Flows of small diameter particle suspensions are common in both environmental and industrial transport problems. One environmental concern is the erosion of topsoil due to irrigation. This leads to the loss of valuable topsoil and to the extraction of pesticides and fertilizers which inevitably enter nearby rivers and lakes. Industrial processes that involve suspension flow include dredging, mining operations and long distance transport of materials by way of pipelines. In most industrial processes, the carrier fluids travel at high enough velocities to disperse the particles uniformly throughout the pipe. However, below limit deposit velocities (Sommerville 1991; Davies 1987) particles move toward the lower portion of the pipe. Here they either settle completely or distribute themselves non-uniformly between the clear carrier fluid and the stationary settled bed where they travel as bed load. Rijn (1984) describes bed load as consisting of rolling and sliding particles that contact the bed very frequently and saltating particles that are ejected upward and travel many particle diameters before again contacting the bed. Garcia & Parker (1991) review a number of models that are intended to predict the entrainment rate for non-cohesive particles. Under many conditions where there is bed load transport, waves can form in the surface of the settled layer. If there is sufficient time, distance and available solids, the waves can grow large enough to clog the pipeline. Kennedy (1963) shows photographs of different wave forms that are observed in settled beds.

While the ability to predict the growth of sand waves *a priori* is an important problem, it is unfortunate that the mechanisms leading to wave formation are in doubt. In addition, while some agreement between experiments and theory have been achieved, there does not seem to be a mathematical formulation that can always predict the conditions where waves form and the resultant wavelength. Wave (or dune or ripple) formation on a settled particle bed has been studied by Bagnold (1956), Richards (1980) and Takahashi *et al.* (1989). Dunes that appear are roughly periodic and travel as trains in the direction of the flow. Typically, researchers have associated the formation of dunes with either turbulence (Williams & Kemp 1971; Richards 1980; Sumer & Bakioglu 1984) or the growth of an existing perturbation on the surface of the bed (Kennedy 1968).

Yalin (1972) states that the growth of dunes is due to a disturbance in the structure of turbulence caused by a discontinuity on the surface. However, our experiments show that sand waves also form on smooth surfaces when the flow is laminar. In order to clarify the conditions for which sand waves form, we examined the formation of sand waves on both sides of the laminar–turbulent transition. We found that there is no observable distinction between the mechanisms which form sand waves at Reynolds numbers across the transition.

Because a flowing sand layer is observed during the sand wave formation process, it is possible that research on the formation of interfacial waves in a two-layer flow consisting of a clear liquid phase and a flowing suspension phase is relevant. Liu (1957) first proposed that the formation of waves on the surface of a particle bed are a consequence of a Kelvin–Helmholtz type instability between two fluids of different densities. Later, Shirasuna (1973) extended this work. In their study of enhanced sedimentation problems, Schaflinger *et al.* (1990) observed the formation of waves at the interface between the resuspended layer of particles and the clear fluid. Zhang *et al.* (1992) modeled this instability as a clear fluid superposed over a suspension with constant physical properties. More recently, Schaflinger (1994) suggested a connection between the formation of interfacial waves in a clear-fluid–suspension flow and the formation of waves in a mono-layer of settled particles.

This paper presents new experimental data on the formation of sand waves in horizontal pipe flow and linear stability analysis of a two-layer flow consisting of a resuspended layer of particles (i.e. suspension phase) and a clear fluid phase within two-dimensional Hagen–Poiseuille flow, as depicted in figure 1. Observations in this study confirm the presence of a separate flowing particle phase on the surface of the particle bed. While it is well known that viscous shear can cause particle resuspension (Leighton & Acrivos 1986), if the suspension phase is too thin or if the particles travel primarily by "rolling" along the surface, representation of the solids phase as a continuum is not assured. Furthermore, there is no guarantee that waves forming on the clear-layer–suspension interface are the cause of, or are related to, sand waves. Linear stability of the clear-liquid–particle phase two-layer flow is addressed here by the use of both constant and spatially varying (corresponding to the increase in particle concentration downward) viscosity profiles. Viscous resuspension theory (Leighton & Acrivos 1986) provides a model for the particle phase. The experimental wavelengths, growth rates and speeds for sand waves do not match predictions from either of the models, indicating that sand waves do not result from an instability of the two-layer flow. However, the measured wavelength increases with Froude number to about the first power suggesting that sand wave formation is related to the behavior of individual sand particles. The measured wavelength is found to agree well with the trajectory flight length for a saltating particle obtained from a model similar to Rijn (1984) for forces on individual particles.

2. EXPERIMENTAL

2.1. Approach

The intent of the experiments was to examine the initial formation of sand waves on the surface of an erodible particle bed for conditions where the clear liquid phase ranges from laminar to

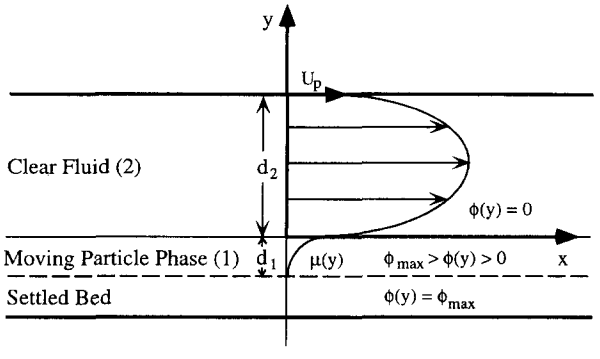

Figure 1. Flow configuration for a two-dimensional Hagen–Poiseuille/Couette flow with a spatially dependent viscosity profile in the lower phase.

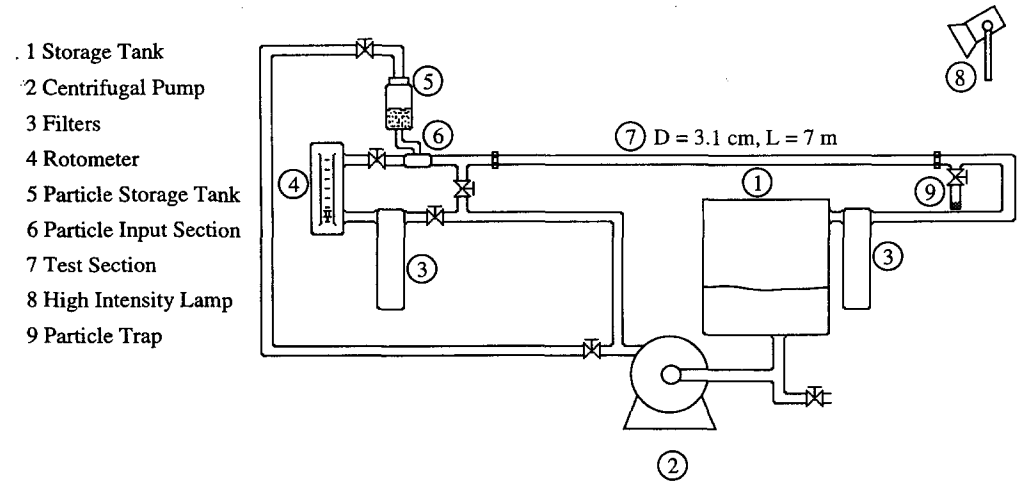

Figure 2. Schematic diagram of the experimental apparatus.

turbulent flow. These experiments produced data on the incipient motion of the particles and on the wavelengths of the first observed waves. The apparatus that is used for this study consists of a pump, a supply tank, a rotameter, a particle input section and a horizontal test section. The test section is a clear acrylic pipe 7 m long and has a diameter of 31.1 mm. Figure 2 shows the apparatus schematically. Although a circular geometry may complicate the problem and the ideal geometry would be a wide rectangular channel, the pipe wall assists experimentation by restraining lateral motion of the particle bed. Because the flowing suspension region is about 2 cm wide and less than 2 mm thick, it is thought that the asymmetric effects of the circular pipe are not significant and the flow is locally two-dimensional. To facilitate easier wavelength measurements, a high intensity lamp is positioned downstream of the wave fronts to cast shadows onto the surface of the bed. Motion of the particles is observed through a rectangular acrylic jacked filled with the carrier fluid to correct for the refraction of light caused by the curvature of the pipe.

The glass particles occupied a small fraction of the area at the bottom of the pipe and would be expected to have minimal effect on the transition to turbulence. This was verified by use of a hot film anemometer. Occasional disturbances in the Laminar flow were observed over most of the range of Reynolds numbers, particularly close to the bottom surface when the waves had grown large. Disturbances occurred more often as the Reynolds number was increased and a signal that looked fully turbulent was observed at a Reynolds number of about 6000. The occurrence of intermittent disturbances in an otherwise laminar flow would be expected because the separation regions behind the wave crests can sometimes detach.

The particles were Cataphote glass spheres with diameters of approximately 100 and 300 μm. A tight particle distribution was assured by sieving the particles between 88 and 106 μm, and 250 and 354 μm sieve trays, respectively. The carrier fluid consisted of mixtures of glycerin and water with viscosities ranging between 1 and 14 cP. The densities of the glass spheres and the carrier fluid were 2.4 and 1.1 g/cm^3, respectively, yielding a density difference $\Delta\rho$ of about 1.3 g/cm^3.

2.2. Results and observations

Mapping the stability regimes for motion of particles and growth of sand waves was undertaken in the first sets of experiments. Figure 3(a) and (b), showing Ψ (Shields parameter $\Psi = \tau/ag\Delta\rho$) versus $\mathrm{Re_p}$ ($\mathrm{Re_p} = 2a\rho_2 v^*/\mu_2$), represent the stability regimes for the 300 and 100 μm spheres, respectively. The term "particle motion" indicates the conditions where sand particles were first observed to be moving. The variable τ is the shear stress on the bed, a is the particle radius, g is gravitational acceleration, $\Delta\rho$ is the density difference between the particles and the carrier fluid, ρ_2 and μ_2 are the density and viscosity of the carrier fluid and v^* is the friction velocity ($v^* = (\tau/\rho_2)^{1/2}$). Shear stresses for the experiments were obtained from friction factor estimates of the Hagen–Poiseuille law for laminar flows and the Blasius formula for turbulent flows. The

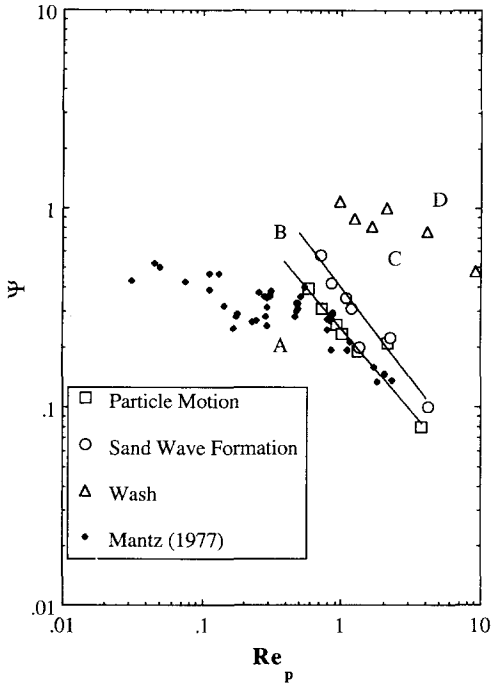

Figure 3(a). Shields diagram for flow regimes of the 300 μm glass spheres. Viscosity increases towards the left.

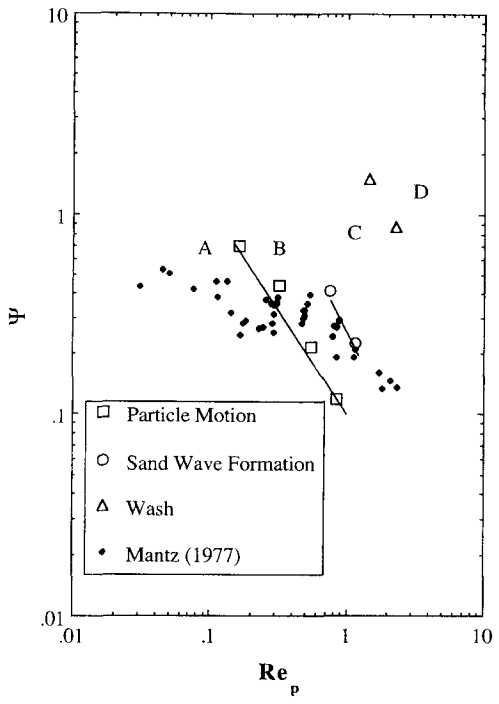

Figure 3(b). Shields diagram for flow regimes of the 100 μm glass spheres. Viscosity increases towards the left.

collected data given by Mantz (1977) for incipient transport of fine cohesionless grains is also included. Mantz's data represent experiments in which the glass spheres and fluids have diameters and viscosities between 15 and 170 μm, and 0.95 and 8 cP, respectively. Our data for incipient particle motion correlate well with the published data for 300 μm glass spheres, while the 100 μm spheres are mixed within the scatter. The slopes of the curves for incipient motion and wave formation in figure 3(a) and (b) are approximately -1. In the absence of inertial effects, the slope is expected to be zero. The deviation from zero slope is consistent with the increased importance of inertia (Cherukat & McLaughlin 1994).

As liquid flow rate is increased, the presence of four regions common to both particle sizes is revealed. The four regimes are as follows: *A*, no particle motion; *B*, particle motion on the surface of the bed without wave formation; *C*, wave formation on the surface of the particle bed; and *D*, destruction of the bed forms. Region *B* represents the motion of the particles from initial rolling to a flowing resuspended layer of particles without the formation of waves on the surface of the bed. The separate flowing suspension phase becomes more definite as the solution viscosity is increased. We should also point out that short wavelength waves were occasionally observed at the interface between the clear fluid and the suspension layer when wave formation was not occurring on the bed. These low amplitude waves are shorter than the initially observed surface waves and their relevance is discussed in section 3.4.

In the second set of experiments, the wavelength distributions of the initially observed surface waves were measured. To produce this data, particles were injected into the test section of the apparatus. A bed of particles approximately 0.5 cm thick in the center and 4–5 m long was obtained by carefully adjusting the individual flow rates and allowing the particles to settle. Each trial was begun by setting the flow rate of the carrier fluid to a specified level; the flow was stopped when sand waves were first observed on the surface of the bed. Visible sand waves, predominately two-dimensional with heights of approximately 2–3 mm, generally grow within a few seconds after the flow begins. Once all possible wavelength measurements were taken, the liquid flow rate was increased high enough to destroy all the bed forms. This routine was repeated until 100 wavelength measurements for the specified conditions were obtained. Results obtained using solutions with viscosities ranging between 1 and 4.3 cP, and 100 and 300 μm glass spheres are presented below.

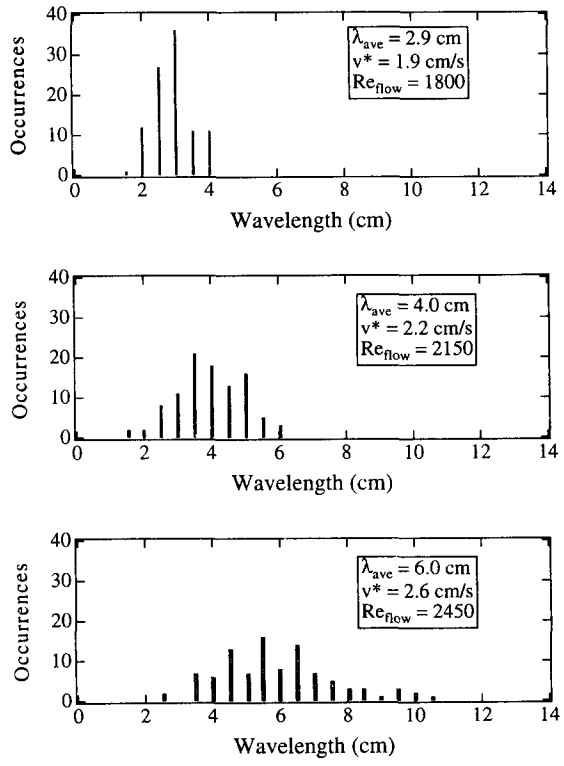

Figure 4. Wavelength distributions as a function of the flow Reynolds number for the 300 μm glass spheres in a 4.3 cP solution.

Figure 4 represents the number of occurrences of a particular wavelength, rounded to a group value, per 100 measurements taken. In this instance, sand waves were found to grow under laminar conditions from an initially flat surface. A similar observation was made by Sumer & Bakioglu (1984), for a flat surface under turbulent flow conditions. Table 1 documents additional results pertaining to distributions of the initially observed wavelengths. In all cases the average wavelength increases with an increase in the flow rate of the carrier fluid. Also, with an increase in the average wavelength there is an increase in the spread of the wavelength distribution, as evidenced by the histograms.

If the flow is maintained, dune growth continues through saturation by way of the erosion of particles from the upstream surface and deposition in the trough. After sufficient time, the dunes gradually detach from each other. Few changes are observed in either speed or shape as they progress downstream, beyond both saturation and detachment. Typically sand waves are two-dimensional but, under high shear and long time intervals, dunes become laterally asymmetric. Their asymmetry causes the downstream path of the suspension phase to mutually oscillate over each wave. Below the point of complete resuspension, this is the most complicated pattern observed.

Table 1. Initial wavelength data

D_p (μm)	μ_2 (cP)	v^* (cm/s)	Re_{flow}	λ_{min} (cm)	λ_{ave} (cm)	λ_{max} (cm)
300	1	1.4	6950	2.0	4.4	7.0
300	1	2.1	10600	3.0	5.0	7.0
300	1	2.3	12000	4.5	7.0	9.5
300	2.2	1.8	3550	2.0	4.1	7.0
300	2.2	2.2	4500	3.0	7.1	12.5
300	2.2	2.3	4800	3.5	9.5	14.0
100	1	1.2	5550	0.8	1.4	2.4
100	1	1.6	7800	0.5	3.3	6.0
100	1	2.1	10600	2.5	5.4	7.0
100	2.1	1.8	3700	1.5	5.2	9.5
100	2.1	2.3	5050	2.5	8.8	12.5

3. LINEAR STABILITY ANALYSIS

The basic supposition of this linear stability analysis is that the problem can be modeled as a two-phase stratified flow. The upper phase is a clear fluid layer and the lower phase is a suspension of particles modeled as a continuum having either a constant or spatially increasing viscosity profile. The lower phase was generalized to include a spatially-varying viscosity because it was desired to reduce, in so far as possible, limitations of the model. For certain conditions, linear stability analysis predicts that waves can form on the interface of the clear-layer–suspension interface. A possible mechanism for the formation of the observed waves in the settled layer, consistent with linear stability analysis of a thin layer, would be that waves form as the result of an instability similar to the slow waves of Craik (1966), where the suspension phase is effectively "piled up". This occurs because the point of maximum shear stress and therefore maximum particle transport occurs upstream of the crest. Deposition will increase downstream of the point of maximum stress and thus particles will be deposited at the crest leading to wave growth.

3.1. Viscosity profile

To perform a two-layer linear stability analysis on a clear fluid superposed over a resuspending layer of particles, an appropriate expression for the viscosity profile in the particle layer is needed. A spatially increasing viscosity profile is suited for this problem because the particle concentration increases downward through the suspension layer. Because the origin of the instability is the viscosity difference between the phases, it is expected that the effect of a viscosity profile will be much more dramatic on the stability characteristics than the effect of a density profile. Therefore density variation in the resuspending layer is not considered. Below, it is shown that density stratification does not significantly affect the outcome of the stability results.

As stated earlier, it is possible to derive a simple analytical model for the suspension viscosity profile using "viscous resuspension" theory (Leighton & Acrivos 1986). Because the particle Reynolds numbers for the experiments are not usually small compared with unity, it is not expected that the model will exactly match the experiments. However, the particle concentration, and therefore the viscosity, will increase downward so that this model will show qualitative differences from a suspension with constant physical properties. Leighton & Acrivos (1986) show that a balance between the shear induced diffusion flux of the particles and the sedimentation flux of the particles governs the resuspension of a layer of sufficiently small particles. The particle flux balance can be written as

$$N_y = -\frac{2}{9}\frac{g\Delta\rho a^2}{\mu_2}\phi f - \hat{D}\dot{\gamma}a^2\frac{\mathrm{d}\phi}{\mathrm{d}y} = 0, \qquad [1]$$

where N_y refers to the flux of particles in the y direction, a is the particle radius, g is the gravitational constant, $\Delta\rho$ is the density difference, f is the hindered settling factor, μ_2 is the viscosity of the carrier fluid and ϕ, $\hat{D}$ and $\dot{\gamma}$ ($\dot{\gamma} = \tau/\mu_r\mu_2$) denote the particle concentration, the dimensionless shear induced diffusion coefficient and the shear rate, respectively. Also, μ_r is the ratio of the viscosity in the suspension to the viscosity of the clear fluid μ_2. When [1] is rendered dimensionless with respect to the viscous resuspension length scale Ψa ($\Psi a = \tau/\Delta\rho g$) and the maximum particle concentration ϕ_{max}, the differential equation becomes

$$\frac{\Psi a}{\phi_{max}}\frac{\mathrm{d}\phi}{\mathrm{d}y} = -\frac{2}{9}\frac{1}{\phi_{max}}\left(\frac{f\phi\mu_r}{\hat{D}}\right). \qquad [2]$$

If the appropriate expressions, given in Chapman & Leighton (1991), for f, $\hat{D}$ and μ_r were substituted into [2], the resulting differential equation would be impossible to solve analytically. Therefore, we approximate the viscosity profile with an exponential function. Figure 5 shows a comparison between the profile obtained from substituting the known correlations (Chapman & Leighton 1991) into [2] and the exponential profile $\mu_r = \exp(-y/\Psi a)$. It is seen that the agreement is good except for the discontinuity in the slope at $y = 0$. This discontinuity in the resuspension model is the result of the shear induced diffusivity vanishing as the particle concentration goes to zero. The exponential increase in viscosity with depth corresponds to the rapid increase in particle

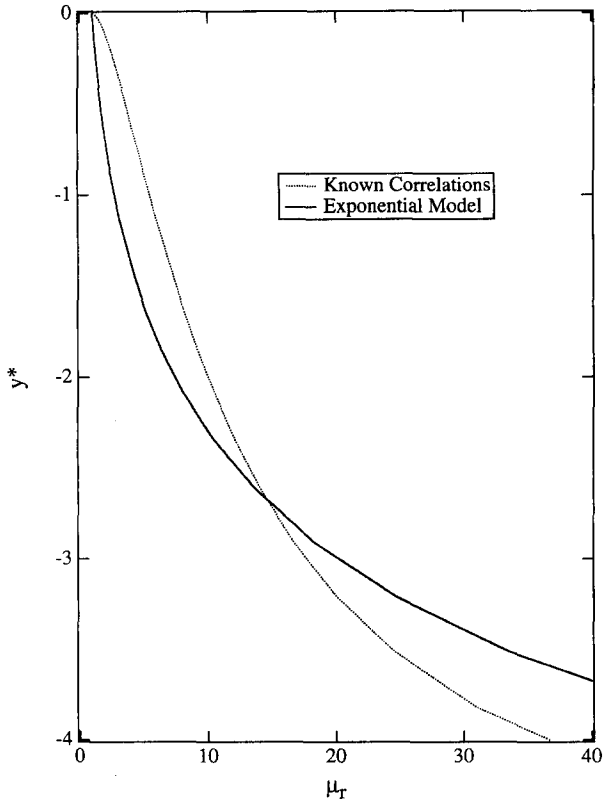

Figure 5. Comparison between the viscosity profiles calculated using both the known correlations and the exponential model.

concentration. To generalize this expression so that it can be used for both constant and spatially varying viscosities, it is convenient to write

$$\mu_r = m \exp(-\beta y\dagger), \qquad [3]$$

where m is the (constant) viscosity ratio between the phases μ_2/μ_1, $y\dagger$ is non-dimensionalized with respect to the thickness of the lower layer d_1, and $\beta = d_1 \Delta\rho g/\tau$, the ratio between the thickness of the suspension layer and the viscous resuspension length scale. This non-dimensionalization scheme follows from an ensuing mathematical formulation of the linear stability problem. For constant viscosity stability calculations $\beta = 0$ and m determines the viscosity ratio between the phases. To produce a spatially varying viscosity profile that does not have a discontinuity across the interface, $m = 1$ and β determines the amplification of the viscosity profile. Since this profile rapidly increases with depth and approaches m as $y\dagger$ tends towards zero, it appears to contain the correct physics and should provide a reasonable model of the suspension layer. The values of m and β corresponding to the fit to [3] given in figure 5 are $m = 1$ and $\beta = 1$, for resuspension at vanishingly small Reynolds numbers. Although the first derivative of the viscosity profile for [3] differs from the more exact result at the interface, the length scale over which the difference occurs is small compared with the depth of the lower phase. Consequently, the difference in the profiles near $y = 0$ would manifest itself only in the short wave instability, which is out of the range of our study.

3.2. Mathematical formulation

Although the experiments cross the laminar–turbulent transition, the base state velocity profiles are modeled as being laminar. These dimensional profiles, $U_1(y)$ and $U_2(y)$, consist of a parabolic profile and a skewed profile:

$$U_2(y) = \left(\frac{-kd_1^2}{2\mu_2}\right)y^2 + C_1 y + C_2, \qquad [4a]$$

$$U_1(y) = \left(\frac{-kd_1^2}{m\beta\mu_2}\right)\exp(\beta y)y + \left(\frac{kd_1^2}{m\beta^2\mu_2} + \frac{C_3}{\beta}\right)\exp(\beta y) + C_4, \quad [4b]$$

where

$$k = -\frac{\partial P}{\partial x}. \quad [5]$$

Here y refers to the vertical coordinate (the same as $y\dagger$ in section 3.1; henceforth the dagger has been dropped) non-dimensionalized with respect to the depth of the lower phase d_1, and C_1, C_2, C_3 and C_4 are constants given in appendix A.

Yih (1967) gives complete details of the derivation of the governing stability equation for the upper phase and all the boundary conditions. Since our derivations are similar, only a few key steps will be presented to illustrate the derivation of the modified lower phase Orr–Sommerfeld equation. The two-dimensional equations, obtained from the Cauchy momentum equations, are written with an arbitrary viscosity profile $\mu(y)$ as

$$u_t + uu_x + vu_y = -P_x - \frac{2\mu}{\mathrm{Re}}u_{xx} + \frac{1}{\mathrm{Re}}\mu_y(u_y + v_x) + \frac{\mu}{\mathrm{Re}}(u_{yy} + v_{yx}), \quad [6a]$$

$$v_t + uv_x + vv_y = -P_y + \frac{\mu}{\mathrm{Re}}(v_{xx} + u_{xy}) + \frac{2}{\mathrm{Re}}(\mu_y v_y + \mu v_{yy}). \quad [6b]$$

These equations are non-dimensionalized with respect to the thickness of the lower layer, the velocity of the interface and the carrier fluid properties. Subscripts indicate partial differentiation with respect to space and time, Re is the Reynolds number ($\mathrm{Re} = \rho_2 d_1 u_0/\mu_2$), u_0 is the interfacial velocity, P is the pressure function and u and v are the velocities in the x and y coordinates, respectively. Next, the velocity and pressure fields are decomposed into primary and perturbation components of motion as

$$u(x, y, t) = U(y) + u'(x, y, t), \quad v(x, y, t) = v'(x, y, t), \quad P(x, y, t) = P(x) + p'(x, y, t). \quad [7]$$

Here the prime indicates perturbation quantities. Note that the viscosity and density fluctuations are taken to be zero. This is because the length scale of small velocity perturbations will be less than a particle radius and therefore should cause no fluctuations in viscosity or density. When [7] is substituted into [6] terms pertaining to the base state flow and quadratic terms arising from the expansion are cancelled. Since we are only considering two-dimensional disturbances, the stream functions χ which solve the continuity equation are given by

$$u' = \frac{\partial \chi}{\partial y}, \quad v' = -\frac{\partial \chi}{\partial x}. \quad [8]$$

The stream function is expanded in terms of a normal mode perturbation:

$$\chi_1(x, y, t) = \phi_1(y)\exp[i\alpha(x - ct)], \quad [9a]$$

$$\chi_2(x, y, t) = \phi_2(y)\exp[i\alpha(x - ct)], \quad [9b]$$

where $\phi_1(y)$ and $\phi_2(y)$ represent the amplitudes of the disturbances, and the non-dimensional parameters, α, c and t, are the wavenumber, complex wave speed and time, respectively. After this final substitution and some reorganization, a modified Orr–Sommerfeld equation for the suspension phase

$$\mu\phi_1^{\mathrm{iv}} + 2\mu'\phi_1''' + (\mu'' - 2\mu\alpha^2)\phi_1'' - 2\mu'\alpha^2\phi_1' + (\mu\alpha^4 + \mu''\alpha^2)\phi_1 = ir\,\mathrm{Re}\,\alpha[(U_1 - c)(\phi_1'' - \alpha^2\phi_1) - U_1''\phi_1] \quad [10a]$$

is obtained. The modified equation includes four additional terms that arise from the spatially dependent viscosity profile. For the clear fluid, the governing stability equation is the following Orr–Sommerfeld equation:

$$\phi_2^{\mathrm{iv}} - 2\alpha^2\phi_2'' + \alpha^4\phi_2 = i\,\mathrm{Re}\,\alpha[(U_2 - c)(\phi_2'' - \alpha^2\phi_2) - U_2''\phi_2]. \quad [10b]$$

Here the prime denotes differentiation with respect to y.

The boundary conditions for this problem include no slip or penetration at the walls, so

$$\phi_1(-1) = \phi_1'(-1) = 0, \quad [11a]$$

$$\phi_2(1/n) = \phi_2'(1/n) = 0. \quad [11b]$$

At the interface, we have the following requirements of continuity in velocity and stress:

$$\phi_1 - \phi_2 = 0, \quad [11c]$$

$$\phi_1' - \phi_2' + (U_1' - U_2')\frac{\phi}{c} = 0, \quad [11d]$$

$$\mu\phi_1'' + \mu\alpha^2\phi_1' - \phi_2'' - \alpha^2\phi_2' + (\mu' U_1' + \mu U_1'' - U_2'')\frac{\phi}{c} = 0, \quad [11e]$$

$$\mu(\phi_1''' - 3\alpha^2\phi_1') + \mu'(\phi_1'' - \alpha^2\phi_1) - (\phi_2''' - 3\alpha^2\phi_2') - \mathrm{Re}\, i\alpha\, \mathrm{Fr}^{-1}(1-r)\frac{\phi}{c} + \mathrm{Re}\, i\alpha(U_1' r - U_2')\phi = \mathrm{Re}\, i\alpha c(\phi_2' - r\phi_1'). \quad [11f]$$

The additional terms in the stress boundary conditions[11e] and [11f] arise from the viscosity profile in the suspension phase. Although the normal stress condition normally includes a surface tension term, there is no surface tension between the clear fluid and the suspension (Zhang *et al.* 1992).

These two stability equations along with the eight boundary conditions constitute a complete eigenvalue problem for the complex wave speed in terms of the physical parameters Re, r, α, n, β and m. For a temporal stability analysis the wavenumber is real and the wave speed complex. If the imaginary part of the complex wave speed is positive, the flow is unstable. Note that a completely rigorous stability analysis would first address the question of absolute versus convective instability. Zhang *et al.* (1992) examined this issue and concluded that this type of flow is convectively unstable but that temporal stability analysis will describe the instability using, if necessary, a Gaster (1962) transformation. Schaflinger (1994) also studied absolute interfacial instability for two superposed fluids.

3.3. Numerical procedure

Several investigators (Zhang *et al.* 1992; Yiantsios & Higgins 1988), using different techniques, obtained the solutions of similar systems of equations for fluids with constant properties. In this study the Chebyshev tau spectral technique (Orszag 1971; Su & Khomami 1992; Gottlieb & Orszag 1977) is used. Orszag (1971) explains that this technique is well suited for the solution of the Orr–Sommerfeld equation as well as other stiff boundary value and eigenvalue problems. Calculating all the eigenvalues of the spectrum with infinite order accuracy and without an initial guess are two advantages of the Chebyshev spectral technique.

The solutions of the governing equations [10a] and [10b] are written as

$$\phi_i(y) = \sum_{n=0}^{N} a_n^{(i)} T_n(y), \quad \text{for} \quad i = 1 \text{ and } 2, \quad [12]$$

where $T_n(y)$ are the Chebyshev polynomials and $a_n^{(i)}$ are the expansion coefficients of each phase (Rivlin 1990). To implement this technique, the stability equations, boundary conditions and base state profiles must be linearly transformed from global coordinates y into localized coordinates ξ_1 and ξ_2. The respective mapping functions for the lower and upper phases are

$$y = \tfrac{1}{2}(\xi_1 - 1) \quad [13a]$$

$$y = \frac{1}{2n}(\xi_2 + 1). \quad [13b]$$

Each governing equation is valid over its localized domain, $-1 \leqslant \xi_i \leqslant 1$, and coupled through the interfacial boundary conditions. Next, the governing equations and boundary conditions are formally expanded in terms of Chebyshev polynomials. Appendix B gives the necessary expansions of the exponential functions. By equating the coefficients of the various $T_n(y)$ to zero, the equations for the expansion coefficients are obtained. To solve for these unknowns, the tau method (Fox &

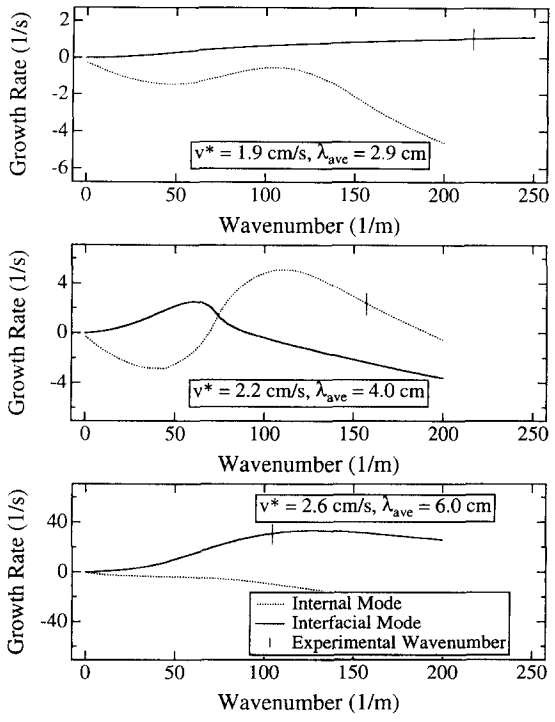

Figure 6. Comparisons between the linear stability predictions of the constant viscosity suspension model and the experimental data for the conditions of figure 4.

Parker 1968) is implemented. This involves the construction of a system of $2(N-3)$ equations which, in combination with the eight boundary conditions and the kinematic condition, gives an algebraic eigenvalue problem consisting of $2(N+3)$ equations. This procedure provides a simple way of transforming the differential eigenvalue problem into an algebraic eigenvalue problem of the form

$$\mathbf{A}\mathbf{x} = \alpha c \mathbf{B}\mathbf{x}, \qquad [14]$$

where $\mathbf{A}$ and $\mathbf{B}$ are coefficient matrices of the expansions, $\mathbf{x}$ is the eigenvector of $a_n^{(j)}$'s and αc is the eigenvalue. This problem is solved for the complex eigenvalue αc using Matlab™.

3.4. Numerical results and comparisons

Figures 6 through 9 represent the numerical results obtained using the Chebyshev tau spectral technique for a suspension with both a constant viscosity and a spatially dependent profile. Common to all these plots is the occurrence of two kinds of unstable modes: interfacial and internal. Yiantsios & Higgins (1988) discriminate these based on the shape of the eigenfunction. The disturbance velocity of the interfacial mode has a maximum at the interface and its streamlines encircle the interface. Conversely, the maximum disturbance of the internal mode is in the middle of the clear phase region and its streamlines are contained between the interface and the upper boundary. Over all wavenumbers, the speed of the interfacial mode is slightly greater than the speed of the interface and the speed of the internal mode is greater than the interfacial mode but less than the maximum upper phase fluid velocity. Both modes are present in the linear stability calculations for both suspension models. The speed of the internal modes indicate that they are disturbances in the clear fluid phase. Because the internal mode is centered in the clear fluid phase, it does not strongly influence the interface. Thus the interfacial mode is more likely than the internal mode to cause a process that leads to wave formation. Results for the internal mode are included for completeness, because the interfacial mode does not correctly predict the measured wavelength as would be expected if the waves form as a result of a two-layer instability.

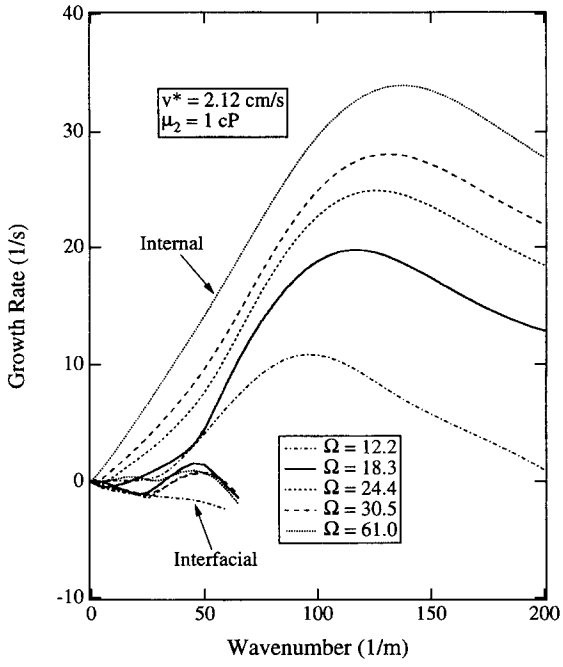

Figure 7. Growth rate versus wavenumber for various values of Ω. Constants are as follows: $\mu_2 = 1$ cP, $v^* = 2.12$ cm/s and $r = 1$.

To implement and compare the two stability models, appropriate values for the depth of the suspension phase are needed. If the viscous resuspension model described above were exactly correct, the depth of the resuspended phase could be calculated. Unfortunately, for a value of $\beta = 1$ (the value corresponding to figure 5), the depth of the particle phase is comparable with a particle radius (for the present parameter ranges), which is not consistent with observations. Because the particle Reynolds number is not small compared with unity, inertial effects enable other lift

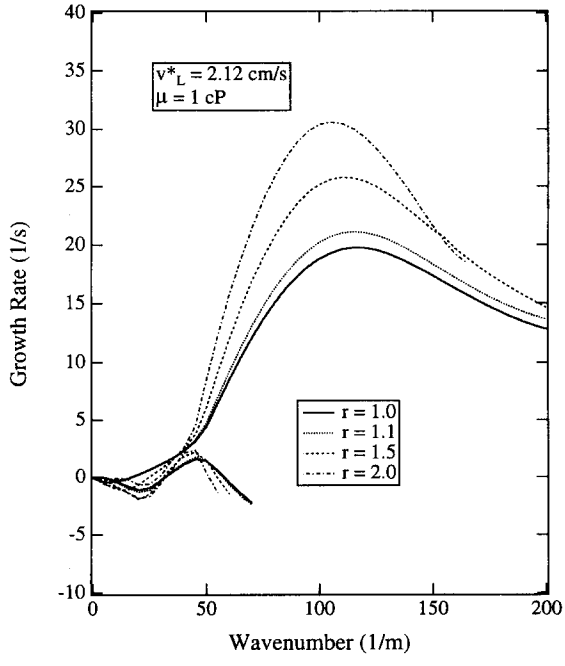

Figure 8. Growth rate versus wavenumber for $r = 1.0$, 1.1, 1.5 and 2.0. Constants are as follows: $\mu_2 = 1$ cP, $v^* = 2.12$ cm/s and $\Omega = 18.3$.

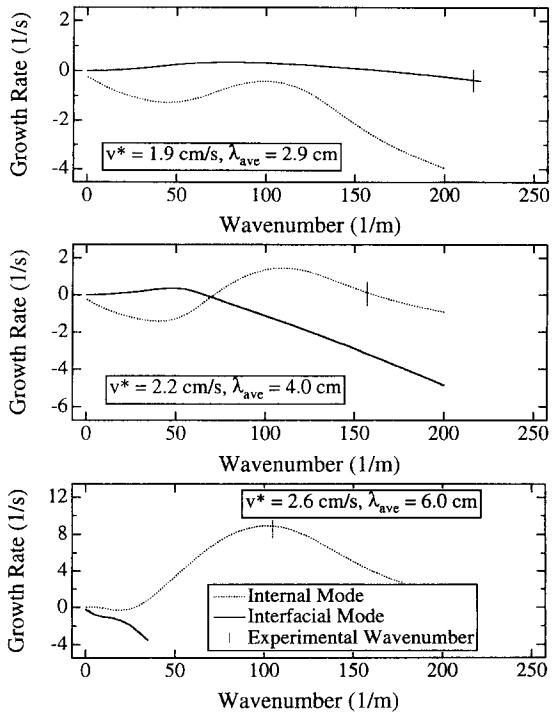

Figure 9. Comparisons between the linear stability predictions of the spatial viscosity suspension model and the experimental data for the conditions of figure 4.

mechanisms making the moving particle phase much thicker than the zero Reynolds number limit. The purely viscous model is effectively a lower bound on the depth of resuspension. It is necessary to use β as an adjustable constant that is obtained from experimental data. It must be emphasized that experimental observations of d_1 are complicated by the difficulty in establishing the exact depth where the solids are no longer moving. Thus experimental depths are accurate to only within about 30%.

First, $\beta_0 (= d_1 \Delta\rho g/\tau)$ is calculated, based on a suspension depth of 1 cm. It was convenient to choose a reference value much deeper than the actual depth of the resuspended layer in our experiments. Next, β is obtained by using

$$\beta = \frac{\beta_0}{\Omega - (1/\mathrm{Re}_p^2)}, \qquad [15]$$

where Re_p is the particle Reynolds number and Ω is an adjustable constant. The form of empirical relation [15] was chosen to give the best representation of the particle phase experimental depths. The constant Ω was adjusted to minimize the error between the correlation [15] and experiments. Equation [15] effectively reduces the number of unknowns from 2, d_1 and β, to a single parameter Ω, which for our calculations is chosen to be 18.3. For a typical trial (shown in table 2), an increase in flow conditions decreases β and increases the depth of the suspension d_1, while the average viscosity increases only slightly. For the constant viscosity calculations, the depth of the lower phase is chosen where the skewed velocity profile is 5% of the interfacial velocity and the integral average of the lower phase viscosity profile is used for the suspension viscosity.

Table 2. Values for the calculation of the physical parameters β, μ_{1ave} and d_1

d (μm)	μ_2 (cP)	v^* (cm/s)	Re_p^2	β_0	β	μ_{1ave}	d_1 (cm)
300	1	1.4	19.4	897	30.0	6.62	0.102
300	1	2.1	40.4	429	14.3	7.07	0.220
300	1	2.3	50.6	343	11.4	7.26	0.278

Table 3. Linear stability comparisons with experimental wavenumbers

Experimental results				Constant viscosity		Spatial viscosity	
D_p (μm)	v^* (cm/s)	λ_{ave} (cm)	α_{ave} (cm^{-1})	α (cm^{-1}) internal	α (cm^{-1}) interfacial	α (cm^{-1}) internal	α (cm^{-1}) interfacial
300	1.4	4.4	140	75	40	80	40
300	2.1	5.0	125	120	35	115	50
300	2.3	7.0	80	125	35	120	50
100	1.2	1.4	450	80	>600	80	190
100	1.6	3.3	190	90	stable	90	35
100	2.1	5.4	115	115	35	110	45

Different values of Ω give slightly different values for the viscosity and depth but these do not substantially change the overall results or comparisons between the models. The effect of various values of Ω on the stability characteristics of the exponential viscosity model is shown in figure 7 and discussed below.

Comparisons between the experimentally observed wavenumbers and the results for a suspension with constant viscosity results are shown in figure 6 and table 3. Figure 6 shows data for 300 μm spheres in a 4.3 cP liquid where the flow is always laminar. It is seen that the measured wavenumber does not correspond to the peak growth rate of the interfacial mode except in the last plot. It likewise does not correspond to the peak of the internal mode. This is the first evidence that questions the possible link between stability analysis and the observed waves. Table 3 shows that similar disagreement exists for other data sets. Consequently, the agreement between experiments and linear theory is not good, suggesting that either the waves do not result from a linear instability or that the spatial variation of suspension properties is very important.

The spatial viscosity model is first explored by varying parameters. Figure 7 illustrates the effect of various values of Ω on the growth rate of the two modes. An increase in Ω results in an increase in the growth rate of the internal mode and no crucial change in the growth rate of the interfacial mode. While the position of the peak of the internal mode changes for various Ω, the more important peak of the interfacial mode does not change. It is likely that the flow becomes turbulent for these cases. Note, however, that a transition to turbulence is possible even when the upper phase is not linearly unstable because channel flow turbulence occurs as the result of a subcritical instability (Drazin & Reid 1981).

Next, the effect of the density ratio r is explored. Figure 8 shows the three most unstable modes for increasing values of the density ratio. An increase in the density ratio slightly decreases the wavenumber of the most unstable internal mode, while the wavenumber of the most unstable interfacial mode remains approximately the same. At constant liquid friction velocity, the growth rate of the interfacial mode increases slightly with an increase in the density ratio. Growth rates of the internal modes change more notably. The effect of the density ratio should be valid for all likely values of particle concentrations in the lower phase. Figure 8 shows that the density ratio has a minimal effect on stability and suggests that omitting density variation from our model is probably justified.

Figure 9 and table 3 show some comparisons between the numerical and the experimental data for the spatial viscosity model. While the theoretical results predict the occurrence of instability, the agreement between the position of the most unstable mode and the experimental wavenumber is lacking. There is again no consistent trend that would suggest a small error in the model resulting from the difference in the geometry. Furthermore, the results for the spatially varying viscosity are no better than the constant viscosity model. Consequently, there is no evidence that the observed waves form from the direct result of a linear instability.

Waves at the interface between the suspension and the clear fluid were observed for some conditions. These are similar to those reported by Schaflinger (1994) who shows some excellent pictures. However these were difficult to capture on video and it was not possible to verify if they were present or not present because of the flow–or because of limited observational ability. It was possible to determine that these waves are much shorter than the waves that first appear on the surface of the bed. They have a wavelength of approximately 1 cm (628 m^{-1}). These may correspond to the interfacial mode of the constant suspension viscosity analysis, but unfortunately

this could not be confirmed because they are much shorter (i.e. have a higher wavenumber) than the first observed waves. Likewise, these would not agree with linear stability.

Further evidence that the stability models do not predict waves is given by the discrepancy in the speeds of the waves compared with predictions. As mentioned above, these values are close to the interfacial speed or the speed of the liquid phase. This could be in the range 5–10 cm/s. Typical speeds for observed waves are approximately 0.08 cm/s so that a serious disagreement exists. While this could be attributed to non-linear effects, the slow rate of travel was observed for waves with very small slopes. One last area of disagreement was the predicted linear growth rates. The calculations indicate that peak linear growth rates ranged from 0.1 to more than 10 s^{-1}. Typical values for experiments were from 10^{-4} to 10^{-3} s^{-1}.

In summary, we find that the sand wave formation process is not consistent with linear wave growth for a two-layer flow. While it could result from limitations in the stability model, it is very likely that wave formation does not occur as the direct result of an instability. Consequently, another approach is needed.

4. SALTATION MODEL FOR WAVELENGTH

Figure 10 shows the experimental wavelength versus Froude number. There seems to be a correlation that closely approximates a line with a slope equal to one. Thus

$$\frac{\lambda}{a} \propto \frac{U^2}{ga}, \qquad [16]$$

where U is the average liquid velocity and λ is the crest-to-crest wavelength. The wavelength is proportional to inertial forces and inversely proportional to gravitational forces. Relation [16] shows that the particle diameter a divides out and does not influence the relation between wavelength, inertia and gravity forces. It is possible that another length scale, such as d_1 which could not be systematically varied or measured, should be used to non-dimensionalize the wavelength. However, this is not available for the present analysis.

Several investigators including Bagnold (1954, 1956), Sumer (1984) and Rijn (1984) have used force balances on individual particles to describe the rate of solids transport. Bagnold (1954) gave a description of how a saltating sand flow in air could lead to dune formation. However, he dismissed this mechanism for sand waves in water. Rijn (1984) predicted individual particle trajectories from

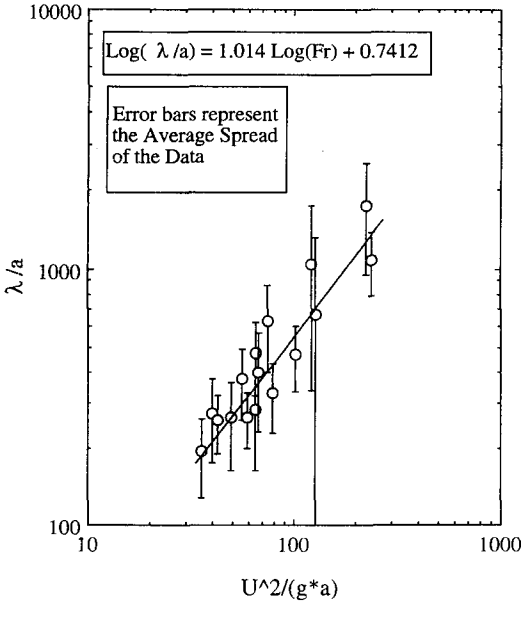

Figure 10. Average wavelength versus particle Froude number.

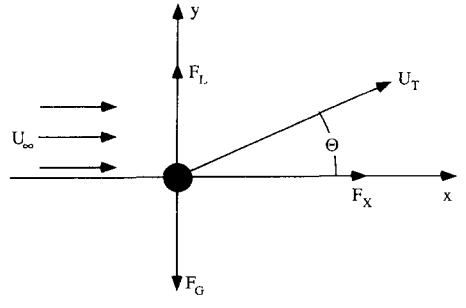

Figure 11. Particle force diagram.

the force balance but no attempt was made to link these to the wavelength of the waves that form—perhaps because he focused on flows too fast for waves to form. The predicted length of trajectories from his model are determined by the gravitational force and the velocity of the flow—consistent with [16]. It is reasonable to propose that the distance that particles travel before "landing" is the preferred wavelength. Thus a trajectory model for individual particles may provide insight into the mechanism of sand wave formation.

Based on these ideas, it is possible to adapt the model of Rijn (1984) to predict the initial wavelength of the sand waves. The primary difference in the present formulation is that the particle is assumed to be in the Stokes regime. Figure 11 represents the forces acting on a single sphere after it is set on a path at velocity U_T, after it leaves the surface of the settled bed. Equations [17], [18] and [19] represent the forces acting on a single sphere.

$$F_L \propto f(F_X), \tag{17}$$

$$F_X = 6\pi a \mu_2 (U_\infty - U_X(t)), \tag{18}$$

$$F_G = \tfrac{4}{3} \Delta\rho g \pi a^3. \tag{19}$$

Here F_L is the lift force on a sphere, F_X is the lateral force, F_G is the gravitational force, U_∞ is the velocity of the fluid approaching the sphere and $U_X(t)$ is the lateral velocity of the sphere at time t. From the force balances, the acceleration on a single sphere in the x and y directions can be calculated. Then, the equations of motion,

$$0 = U_{y0} + \tfrac{1}{2} a_y t, \tag{20}$$

$$\lambda = U_{x0} t + \tfrac{1}{2} a_x t^2, \tag{21}$$

are solved for the distance λ traveled in the x-direction, giving

$$\lambda = \frac{2\rho_s U_{x0} U_{y0}}{\Delta\rho g} + \tfrac{1}{2} a_x \left(\frac{2\rho_s U_{y0}}{\Delta\rho g} \right)^2. \tag{22}$$

In these equations, the terms a_x and a_y represent the particle acceleration in the x and y directions, respectively. If $U_X(t) \to U_\infty$, which should be valid for both large t and spheres that are already in rolling motion, there will be no acceleration in the x direction. Therefore, [22] simplifies to give the following expression for the distance traveled by the sphere:

$$\lambda = \frac{2\rho_s U_{x0} U_{y0}}{\Delta\rho g}. \tag{23}$$

The velocity components U_{x0} and U_{y0} can be expressed in terms of U_T to give

$$\frac{\lambda}{a} = \left(\frac{2\rho_s \sin\theta \cos\theta}{\Delta\rho} \right) \frac{U_T^2}{ag}. \tag{24}$$

Equation [24] shows that the distance a particle travels is proportional to the square of the particle velocity and inversely proportional to the gravitational force on the particle. Using the slope of λ/a versus $(2\rho_s/\Delta\rho)U^2/ag$ from figure 10, which is approximately 0.287, the particle ejection angle is approximately 17.8°.

5. DISCUSSION AND SUMMARY

For the systems studied, experiments show that a flowing particle phase occurs on top of the settled bed and that periodic waves form on the bed. Based on studies by Liu (1957), Shirasuna (1973), Schaflinger *et al.* (1990), Zhang *et al.* (1992) and Schaflinger (1994), a possible explanation for this process is that the two-layer flow is unstable and that the waves are the manifestation of growth of the instability. Linear stability analysis using a constant viscosity model predicts that the two-layer flow is unstable because the viscosity of the two layers is different. However, measured values of the wavelength show no consistent relation to the predicted wavelength. A second model for the flow, which has a continuous viscosity across the interface but a variable viscosity with depth, exhibits somewhat different stability predictions than the constant model but no better

agreement with the data. It would be possible to derive more elaborate relations for the particle density and therefore the viscosity and density profiles in the suspension phase. However, it seems unlikely that changing these profiles would predict the data much better. It could be that the very thin moving particle phase, where the particles have saltation trajectories, cannot be accurately represented by a continuum model. In addition, as we have seen throughout our experimental results, the wavelength of the sand waves which first appear increases with flow rate of the carrier fluid. This is the opposite of the trend that is expected using linear stability analysis. If it is still desirable to pursue the link between sand waves and the two-layer instability, another possibility is to model the suspension phase with a viscosity that is shear dependent. However, Schaflinger (1994) gives sound reasons, backed up with experiments and calculations, why this should not be necessary.

Schaflinger (1994) states that the wavelength of the ripples formed in a *monolayer* of particles sheared by a laminar flow corresponds to the predictions of his two-layer stability analysis. His result refutes, to some extent, our concern about the correctness of representing the lower phase as a continuum. Because his experiments are not described in detail, it is not completely clear if they are comparable with the present study. His value of $\Delta\rho/\rho_s$ is about 0.007, which is much smaller than the value of 0.58 for the present experiments. As a consequence, there would be much less saltation in his experiments compared with the present ones. We could not see if ripples form on the top layer of settled particles in our experiments. However if they do, they do not lead to the larger amplitude waves that occur in the settled layer.

The likely scenario for the wave formation process is as follows. Once the two layers are flowing, the interface is unstable to short waves. These try to form but are limited to very small amplitude because the suspension phase has no surface tension. This means that protrusions of high particle concentration into the clear fluid phase are washed out because the clear fluid is moving faster. The mechanism for formation of waves in the settled bed is the saltation mechanism described above. Shearing the stationary particle bed causes resuspension and imparts an upward velocity with a definable trajectory angle. This leads to a preferred wavelength for the formation of sand waves. This mechanism suggests an interesting effect once the waves attain a sufficiently large amplitude. The slope of the waves will increase the ejection angle. A larger angle will cause longer flight distance which will cause the waves to travel and eventually cause the wavelength to increase. Both of these events are observed in the experiments.

The trajectory model presented here omits some potentially important effects and cannot predict the key variable: the ejection angle. More elaborate analysis might provide some insight, as might more precise resuspension experiments. However, the experiments in this study demonstrate that formation of sand waves is consistent with a particle saltation mechanism and not with linear stability analysis of the two-layer flow.

Acknowledgement—This work was supported in part by Amoco Oil Corporation.

REFERENCES

Bagnold, R. A. 1954 *The Physics of Blown Sand and Desert Dunes*. Methuen, London.

Bagnold, R. A. 1956 The flow of cohesionless grains in fluids. *Proc. R. Soc. A* **249,** 235–297.

Chapman, B. & Leighton, D. T. 1991 Dynamic viscous resuspension. *Int. J. Multiphase Flow* **17,** 469–483.

Cherukat, P. & McLaughlin, J. B. 1994 The inertial lift on a rigid sphere in a linear shear flow field near a flat wall. *J. Fluid Mech.* **263,** 1–18.

Craik, A. D. D. 1966 Wind generated waves in thin liquid films. *J. Fluid Mech.* **26,** 369–392.

Davies, J. T. 1987 Calculation of critical velocities to maintain solids in suspension in horizontal pipes. *Chem. Engng Sci.* **42,** 1667–1670.

Drazin, P. G. & Reid, W. H. 1981 *Hydrodynamic Stability*. Cambridge University Press.

Fox, L. & Parker, I. B. 1968 *Chebyshev Polynomials in Numerical Analysis*. Oxford University Press.

Garcia, M. & Parker, G. 1991 Entertainment of bed sediment into suspension. *J. Hydraul. Engng* **117,** 414–435.

Gaster, M. 1962 A note on the relation between temporally-increasing and spatially-increasing distrubances in hydrodynamic stability. *J. Fluid Mech.* **14,** 222–224.
Gottlieb, D. & Orszag, S. A. 1977 *Numerical Analysis of Spectral Methods: Theory and Applications.* SIAM, Philadelphia, PA.
Hanratty, T. J., & McCready, M. J. 1995 Phenomenological understanding of separated gas–liquid flows. *Multiphase Science and Technology.* In press.
Kennedy, J. F. 1963 The mechanics of dunes and antidunes in erodible-bed channels. *J. Fluid Mech.* **16,** 521–544.
Leighton, D. & Acrivos, A. 1986 Viscous resuspension. *Chem. Engng Sci.* **41,** 1377–1384.
Liu, H. K. 1957 *Proc. Am. Soc. civ. Engng* **95,** 1835.
Mantz, P. A. 1977 Incipient transport of fine grains and flakes by fluids–extended Shields diagram. *J. Hydraul. Div.* June 1977, 601–615.
Orszag, S. A. 1971 Accurate solution of the Orr–Sommerfeld stability equation. *J. Fluid Mech.* **50,** 689–703.
Richards, K. J. 1980 The formation of ripples and dunes on an erodible bed. *J. Fluid Mech.* **99,** 597–618.
van Rijn, L. C. 1984 Sediment transport, part 1: Bed load transport. *J. Hydraul. Engng* **110,** 1431–1456.
Rivlin, T. J. 1990 *Chebyshev Polynomials: From Approximation Theory to Algebra and Number Theory*, 2nd edn. Wiley–Interscience, New York.
Schaflinger, U. 1994 Interfacial instabilities in a stratified flow of two superposed fluids. *Fluid Dynam. Res.* **13,** 299–316.
Schaflinger, U., Acrivos, A. & Zhang, K. 1990 Viscous resuspension of a sediment within a laminar and stratified flow. *Int. J. Multiphase Flow* **16,** 567–578.
Shirasuna, A. S. 1973 Formation of sand waves. *Proc. 15th Cong. Int. Assoc. Hydraul. Res.* **1,** 107–114.
Sommerville, D. R. 1991 Critical transport velocity in two-phase, horizontal pipe flow. *AIChE Jl* **37,** 274–276.
Su, Y. Y. & Khomami, B. 1992 Numerical solution of eigenvalue problems using spectral techniques. *J. Comput. Phys.* **100,** 297–305.
Sumer, B. M. 1984 Lift forces on moving particles near boundaries. *J. Hydraul. Engng* **110,** 1272–1278.
Sumer, B. M. & Bakioglu, M. 1984 On the formation of ripples on an erodible bed. *J. Fluid Mech.* **144,** 177–190.
Takahashi, H., Masuyama, T. & Noda, K. 1989 Unstable flow of a solid–liquid mixture in a horizontal pipe. *Int. J. Multiphase Flow* **15,** 831–841.
Williams, P. B. & Kemp, P. H. 1971 *Boundary-Layer Met.* **11,** 439.
Yalin, M. S. 1972 *Mechanics of Sediment Transport.* Pergamon Press, Oxford.
Yiantsios, S. G. & Higgins, B. G. 1988 Linear stability of plane Poiseuille flow of two superposed fluids. *Phys. Fluids* **31,** 3225–3238.
Yih, C. S. 1967 Instability due to viscosity stratification. *J. Fluid Mech.* **27,** 337–352.
Zhang, K., Acrivos, A. & Schaflinger, U. 1992 Stability in a two-dimensional Hagen–Poiseuille resuspension flow. *Int. J. Multiphase Flow* **18,** 51–63.

APPENDIX A

In this appendix we present equations for the coefficients of the base state velocity profiles:

$$C_1 = (-2An^2 - 2A\beta n^2 + 2An^2\exp(\beta) - A\beta^2\exp(\beta)m + 2\beta^2 n^2\exp(\beta)mU_p)/D, \quad [A1]$$

$$C_2 = (A\beta + 2An + 2A\beta n - A\beta\exp(\beta) - 2An\exp(\beta) - 2\beta n^2 U_p + 2\beta n^2\exp(\beta)U_p)/D, \quad [A2]$$

$$C_3 = (2An^2 - 2A\beta n^2 - 2An^2\exp(\beta) - A\beta^2\exp(\beta)m - 4A\beta n\exp(\beta)m + 2\beta^2 n^2\exp(\beta)mU_p)/(mD), \quad [A3]$$

$$C_4 = (2An^2 + A\beta m + 2Anm + 2A\beta nm - 2\beta n^2 mU_p)/(mD), \quad [A4]$$

where

$$D = 2\beta n(-n + n\exp(\beta) + \beta\exp(\beta)m), \tag{A5}$$

and

$$A = -kd_1^2/\mu_2. \tag{A6}$$

APPENDIX B

In this appendix we present some of the necessary expansions for the solution of our linear stability problem. Let the Chebyshev expansion of the disturbance amplitude functions $\phi(x)$ be given by

$$\phi(y) = \sum_{n=0}^{\infty} a_n T_n(y). \tag{B1}$$

Chebyshev polynomials are represented by $T_n(y)$ and a_n represents the expansion coefficients. We can further expand functions of $\phi(x)$ in terms of the linear operator **L**, as follows:

$$\mathbf{L}\phi(y) = \sum_{n=0}^{\infty} b_n T_n(y). \tag{B2}$$

Here b_n represents the expansion coefficients under the linear operator **L**. Most of the necessary Chebyshev polynomial expansions required for the solution of this eigenvalue problem are given in Orszag (1971). Here we present only the additional expansions required due to the exponential viscosity profile in the lower phase. Derivatives of the disturbance amplitude function are given first. Then, we consider the Chebyshev expansions for the exponential function and the products of the exponential function with other functions.

Since Orszag (1971) derives the Chebyshev expansions for the derivatives of $\phi(y)$, we do not present them here. However, we need an expansion for $\phi'''(y)$. The coefficients for the expansion of the third derivative are given by the following:

$$c_n b_n = \sum_{\substack{p=n+3 \\ p+n \equiv 1 (\mathrm{mod}\ 2)}}^{\infty} \frac{p(-1-n+p)(1-n+p)(-1+n+p)(1+n+p)}{4} a_p. \tag{B3}$$

Here $c_n = 0$ if $n < 0$, $c_0 = 2$, and $c_n = 1$ if $n > 0$.

It can be shown from the inner product relation by Chebyshev polynomials that the coefficients of the exponential function are given by the following:

$$\exp(cy) = \sum_{n=0}^{\infty} B_n T_n(y), \tag{B4}$$

where

$$B_n = \frac{2}{c_n} \sum_{j=0}^{\infty} \frac{c^{2j+n}}{2^{2j+n} j!(j+n)!} = \frac{2i^n}{c_n} J_n(-ci). \tag{B5}$$

Here J_n is the first Bessel function of order n. If we write the expansion for any function $\phi(y)$ as $\mathbf{L}\phi(y) = \Sigma_{n=0}^{\infty} A_n T_n(y)$, we can write the product of two functions as follows:

$$\exp(cy)\phi(y) = \sum_{m=0}^{\infty} \sum_{n=0}^{\infty} A_n B_m T_n(y) T_m(y). \tag{B6}$$

Here we can use the relation for the product of two Chebyshev polynomials [B6], to expand the product of the two Chebyshev polynomials.

$$T_n(y)T_m(y) = \tfrac{1}{2}[T_{n+m}(y) + T_{|n-m|}(y)]. \tag{B7}$$

It may be shown that the product of the exponential function with a Chebyshev expansion of some function $\phi(y)$ is given by

$$\exp(cy)\mathbf{L}\phi(y) = \sum_{n=0}^{\infty} \left[\sum_{m=0}^{\infty} (\tfrac{1}{2} d_{n-m} A_{n-m} B_m + \tfrac{1}{2} d_{m-n} A_{m-n} B_m + \tfrac{1}{2} d_{n-1} A_{n+m} B_m) \right] T_n(y), \tag{B8}$$

where $d_n = 0$ if $n \leqslant 0$ and $d_n = 1$ otherwise. This relation may be used for all the necessary products of exponentials and linear operators of $\phi(y)$ in this problem.